9

Research Article

Liping Xu, Jiangtao Xu, Xin Yao, Rumin Zhang, Gang Wen, Lei Wang, Xingxing Lu, Zaoxia Li, Wenquan Liu, Dongshan Wei, Xiaoli Li, Tianying Chang* and Hong-Liang Cui

Quantum weak value amplified terahertz chiroptical measurement

https://doi.org/10.1515/nanoph-2024-0685 Received November 27, 2024; accepted March 27, 2025; published online April 16, 2025

Abstract: A precise method for phase and amplitude detection in both the time and frequency domains of terahertz spectroscopy based on the weak-value amplification technique is proposed and demonstrated. Within the weakvalue amplification scheme, the imaginary weak value enhances variations in the terahertz phase signals, whereas the real weak value amplifies changes in the terahertz amplitude signals. By employing various postselections in the terahertz weak measurement procedure in detecting minute changes of the phase and amplitude of the terahertz wave, we achieved a phase change range from -0.0187 rad to 0.0183 rad with an interval of 0.004 rad and an amplitude change range from -0.0238 rad to 0.0228 rad with an interval of 0.0056 rad. This results in a phase and amplitude measurement resolution of 10^{-4} rad in the time domain. In the frequency domain, |E| spectra are calculated to assess phase and amplitude variations with respect to frequency or wavelength. We apply these methods to chiral detection, particularly in measuring optical activity such as circular dichroism (CD) and optical rotatory dispersion (ORD). Despite challenges such as strong terahertz wave absorption in aqueous solutions and weak optical responses from natural chiral materials in the terahertz band, we successfully conducted chiroptical spectroscopy on a relatively large volume (2.3 mL) of liquid (R)- and (S)-limonene, as well as

lactose tablets with varying mass fractions. Furthermore, the carrier-envelope phase (CEP) shift, defined for one-or few-cycle time-domain terahertz pulses, was effectively achieved through the manipulation of a pair of terahertz polarizers in the terahertz beam path. Notably, when $\phi_{\text{CEP}}=0$, a 150 % increase in the absorption coefficient of lactose was observed when weak measurement techniques were employed, compared to conditions without such measurements. This effort yielded THz-ORD and THz-CD spectra, demonstrating the potential of our methods to overcome traditional limitations and provide new insights into the optical response, dynamic properties, and low-frequency vibrational modes of biomolecules and materials in low-energy states, ultimately facilitating the identification of chiral stereoisomers.

Keywords: THz; phase; amplitude; chirality; optical activity; weak-value amplification

1 Introduction

Terahertz waves (THz) refer to electromagnetic waves with frequencies ranging from 0.1 to 10 THz, bridging the gap between microwave and infrared radiation [1], [2]. THzbased detection technology shows great potential due to its distinctive physical traits, including fingerprint spectral specificity, water sensitivity, nonionization, broadband, strong coherence, and low photon energy, setting it apart from other bands of the electromagnetic wave spectrum [3], whereas, as with other electromagnetic wave based spectroscopies, THz detections are typically characterized by the electric field vectors in complex representations of both amplitude and phase. Polarization is also a fundamental characteristic of electromagnetic waves, describing the vector nature of their electric field oscillations. The relative variations in the phase and amplitude of polarized THz wave basis vectors arise from distinct physical mechanisms: phase differences occur due to variations in the propagation velocities of the eigenvectors influenced

Liping Xu, Jiangtao Xu, Xin Yao, Rumin Zhang, Gang Wen, Lei Wang and Xiaoli Li, The College of Nuclear Technology and Automation Engineering, Chengdu University of Technology, Chengdu, Sichuan 610059, China

Xingxing Lu, Zaoxia Li, Wenquan Liu, Dongshan Wei and Hong-Liang Cui, Shenzhen Institutes of Advanced Technology, Chinese Academy of Sciences, Shenzhen, Guangdong 518055, China

^{*}Corresponding author: Tianying Chang, Shenzhen Institutes of Advanced Technology, Chinese Academy of Sciences, Shenzhen, Guangdong 518055, China, E-mail: ty.chang@siat.ac.cn. https://orcid.org/0000-0001-5635-9547

by the medium's refractive index, while amplitude variations result from deviations in the absorption coefficients due to the medium's differential attenuation characteristics [4]. Flexible manipulations or estimations of the physical properties (amplitude and phase) of the THz polarization state provide key support for THz application systems in multichannel communication, beam tracking and radar detection, polarization imaging, and chiral detection of biomolecules, among others [1], [5], [6].

Optical chiral detection, probing the optical chiral response of molecules interacting with left- and rightcircularly polarized waves, is primarily manifested as CD and ORD [7], [8]. This response elucidates the mechanisms of ORD and CD, which correspond to the phase and amplitude variations of the incident light, respectively [1], [4], [9]. These techniques are widely used to analyze biomacromolecules, such as proteins and nucleic acids, in the ultraviolet and visible light regions (200-800 nm). In contrast, vibrational optical activity, which includes vibrational circular dichroism and vibrational optical rotation, is observed in the infrared and far-infrared regions (1,000-100,000 nm). This method is utilized for analyzing molecular structure and vibration modes. Analyzing low-frequency vibrations and rotational characteristics at THz wavelengths poses significant challenges. The THz wavelength greatly exceeds that of typical chiral molecular structures, leading to weaker chirality of natural materials in this regime, which complicates the study of chiral properties in biomolecules and low-energy materials [10]-[12]. Additionally, strong absorption of THz waves by water molecules further impairs the precision and sensitivity of traditional THz spectroscopy in aqueous solutions. Recently, THz artificial microstructure devices (e.g., metasurfaces, subwavelength gratings, and photonic liquid crystals) have emerged, introducing geometric symmetry breaking to enhance THz chiral responses efficiently [1]. The chiral effect induced by these artificial structures surpasses that of natural materials by several orders of magnitude. Unlike metamaterials and metasurfaces, which have fixed chiral responses upon fabrication, photonic liquid crystals offer dynamic tunability through thermal, optical, electric, or magnetic field control [1], [13]. However, metamaterials, metasurfaces, and liquid crystals primarily focus on maximizing phase change, with some capable of achieving changes from -150° to 145° [1], [13], [14]. In summary, due to the strong absorption of terahertz waves in aqueous solutions and the weak optical response of natural chiral materials in the terahertz band, particularly concerning optical chiral responses, achieving the measurement of liquid natural chiral materials requires detecting unusually small changes in phase and amplitude, which ultimately facilitates the identification of chiral stereoisomers.

The advent of weak-value amplification (WVA) represents a transformative breakthrough in overcoming these challenges. Initially proposed by Aharonov, Albert, and Vaidman in 1988, WVA has emerged as a powerful tool in high-precision metrology [15]. Its unique ability to enhance signal variations while mitigating technical noise has made WVA indispensable for the precise measurement of subtle parameters [16]-[31]. This remarkable amplification capability extends to diverse applications, including polarization rotations [32], [33], optical phases [32], [34], [35], chemical reaction rate [36], and more.

In this study, we developed a method that integrates THz systems with quantum weak measurements. Experimentally, we simultaneously estimated phase and amplitude variations in both time and frequency domain. Our findings demonstrate that the imaginary weak value is responsible for amplifying the THz wave phase shifts. enhancing our ability to detect minute changes in the propagation velocities of the eigenvectors. On the other hand, the real weak value amplifies the THz waves amplitude variations, allowing for precise measurement of differential absorption coefficients. Employing this approach, we successfully conducted chiroptical spectroscopy on liquid (R)and (S)-limonene and lactose tablets with different mass fractions, yielding THz-ORD and THz-CD spectra crucial for chiral detection. These experimental outcomes underscore the system's exceptional accuracy and practical feasibility.

2 Theoretical model

Creating a theoretical framework for establishing THz wave phase and amplitude based on WVA begins with preselecting the initial THz photon polarization state in a superposition of eigenstates

$$\left|\psi_{\rm pre}\right\rangle = \frac{1}{\sqrt{2}}(\left|H\right\rangle + \left|V\right\rangle),\tag{1}$$

where $|H\rangle$ and $|V\rangle$ denote the horizontal and vertical polarization eigenstates, respectively.

Small variations in the phase α and amplitude β are encapsulated by the interaction/evolution operator

$$\widehat{U}_{(\alpha)} = \exp\left(\frac{i\alpha}{2}\widehat{A}\right),\tag{2}$$

$$\widehat{U}_{(\beta)} = \exp\left(\frac{\beta}{2}\widehat{A}\right),\tag{3}$$

where $|H\rangle$ and $|V\rangle$ are the eigenvectors of photon polarization operator $\hat{A} = |H\rangle\langle H| - |V\rangle\langle V|$, which denotes the

observable of the system, i.e., the THz photon polarization in the present case.

To estimate the phase variation, the postselection state is

$$\left|\psi_{\text{post}(\alpha)}^{\pm}\right\rangle = \frac{1}{\sqrt{2}} \left[\exp(\mp i\kappa)|H\rangle - \exp(\pm i\kappa)|V\rangle\right],$$
 (4)

± represents the two symmetric (with respect to the exact perpendicular direction of the preselected polarization direction) postselection states.

According to the general weak value expression [34], the imaginary weak value is derived from the preselected and postselected states

$$A_{w(\alpha)}^{\pm} = \frac{\left\langle \psi_{\text{post}(\alpha)}^{\pm} \middle| \hat{A} \middle| \psi_{\text{pre}} \right\rangle}{\left\langle \psi_{\text{post}(\alpha)}^{\pm} \middle| \psi_{\text{pre}} \right\rangle} = \mp i \cot \kappa. \tag{5}$$

The intensity of the THz wave after postselection corresponding to the state is given by

$$\begin{split} I_{\alpha}^{\pm} &= I_{0} \left| \left\langle \psi_{\text{post}(\alpha)}^{\pm} \middle| \widehat{U}_{(\alpha)} \middle| \psi_{\text{pre}} \right\rangle \right|^{2} \\ &\approx I_{0} \left| \left\langle \psi_{\text{post}(\alpha)}^{\pm} \middle| \psi_{\text{pre}} \right\rangle \right|^{2} \left[1 - \alpha \text{Im}(A_{w}) \right] \\ &= I_{0} \sin^{2} \kappa \left[1 - \alpha \text{Im} \left(A_{w(\alpha)}^{\pm} \right) \right], \end{split} \tag{6}$$

where I_0 denotes the initial THz spectrum intensity prior to postselection. The approximation in eq. (6) is valid when $\left|A_{w(\alpha)}^{\pm}\right|^{2}(\alpha^{2})/4\ll 1.$

To estimate the amplitude variation, the postselection

$$\left|\psi_{\text{post}(\beta)}^{\pm}\right\rangle = \cos\left(\frac{\pi}{4} \mp \chi\right)|H\rangle - \sin\left(\frac{\pi}{4} \mp \chi\right)|V\rangle,$$
 (7)

and according to the weak value expression, the real weak value is derived from the preselected and postselected states

$$A_{w(\beta)}^{\pm} = \frac{\left\langle \psi_{\text{post}(\beta)}^{\pm} \middle| \widehat{A} \middle| \psi_{\text{pre}} \right\rangle}{\left\langle \psi_{\text{post}(\beta)}^{\pm} \middle| \psi_{\text{pre}} \right\rangle} = \pm \cot \chi. \tag{8}$$

The intensity of the THz wave after postselection corresponding to the state is given by

$$I_{\beta}^{\pm} = I_{0} \left| \left\langle \psi_{\text{post}(\beta)}^{\pm} \middle| \widehat{U}_{(\beta)} \middle| \psi_{\text{pre}} \right\rangle \right|^{2}$$

$$\approx I_{0} \left| \left\langle \psi_{\text{post}(\beta)}^{\pm} \middle| \psi_{\text{pre}} \right\rangle \right|^{2} \left[1 + \beta \text{Re} \left(A_{w(\beta)}^{\pm} \right) \right]$$

$$= I_{0} \sin^{2} \chi \left[1 + \beta \text{Re} \left(A_{w(\beta)}^{\pm} \right) \right], \tag{9}$$

where, I_0 denotes the initial THz spectrum intensity before postselection. In eq. (9), the approximation is based on the condition that $\left|A_{w(\beta)}^{\pm}\right|^2(\beta^2)/4 \ll 1$. From eq. (9), it is seen that the postselected THz wave intensity diminishes according to the probability of selection $\sin^2 \chi$, with the intensity alteration being proportional to the weak value.

3 Results and discussion

A simplified schematic of the THz setup utilizing weak-value amplification to capture phase and amplitude variation data in a transmission configuration is illustrated in Figure 1. The THz emitter and detector are horizontal polarization and copolarized. Figure 1a depicts the WVA segment highlighted in color along the entire optical path. Initially, the THz wave passes through the first THz polarizer 1 (Product model: PWO0S-012-050, THz wire grid polarizers, wavelength range above 150 μm, extinction ratio >1,000:1, TYDEX Co., Russia) and subsequently interacts with the first THz quarter-wave plate (QWP1, Product model: WP-CQ-D50-0W118.8-L/4, Operation wavelength range 40-1,000 µm, Material THz grade crystal quartz, TYDEX Co., Russia), collectively serving as the preselection components. These elements are aligned with their optical axes both at $\pi/4$ relative to the horizontal direction. By adjusting THz polarizer 1 relative to QWP1, small phase variations between the horizontal and vertical polarization components are induced. For postselection, we utilize the second THz quarter-wave plate (QWP2, Product model: WP-CQ-D50-0W118.8-L/4, Operation wavelength range 40-1,000 μm, Material THz grade crystal quartz, TYDEX Co., Russia) and the second THz polarizer 2 (Product model: PWO0S-012-050, THz wire grid polarizers, wavelength range above 150 μ m, extinction ratio >1,000:1, TYDEX Co., Russia), both oriented at $-\pi/4$ relative to the horizontal direction. Rotation of THz polarizer 2 facilitates the construction of the postselection process described in eq. (4), yielding an imaginary weak value as detailed in eq. (5). The postselected THz wave is then detected using a THz detector to estimate phase variations.

In Figure 1b, the colored section signifies the quantum weak measurement segment along the entire optical path, which is the same optical path depicted in Figure 1a sans the two quarter-wave plates. Here, the THz wave first encounters the preselection component THz polarizer 1, with its optical axis set at an angle of $\pi/4$ relative to the horizontal direction. Adjusting THz polarizer 1 induces minute amplitude variations between horizontal and vertical polarization components. For postselection, we employ the second THz polarizer 2, aligned at $-\pi/4$ relative to the horizontal direction. By adjusting THz polarizer 2, the postselection process described in eq. (7) is established, resulting in a

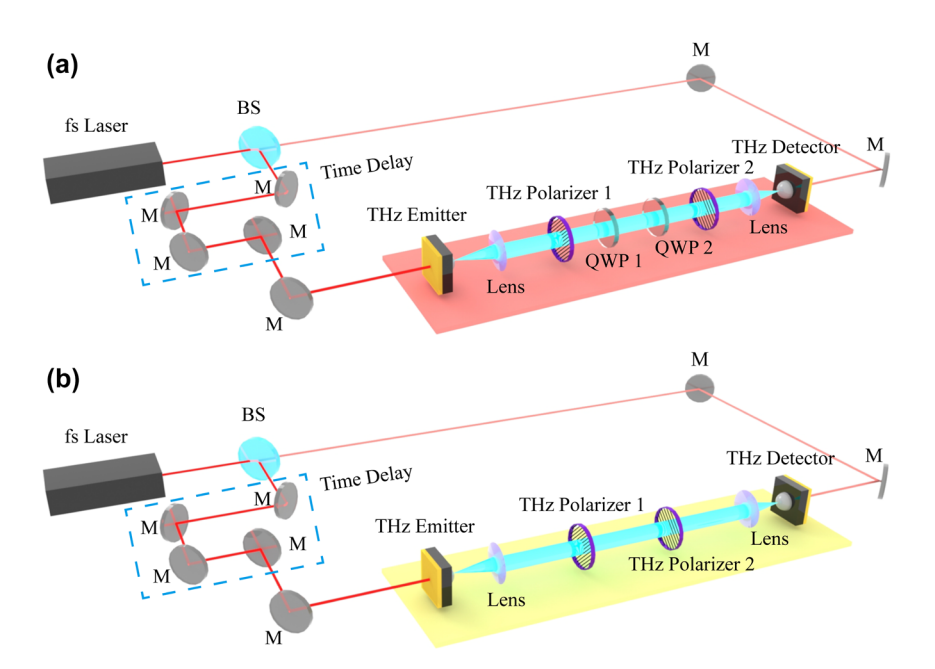


Figure 1: A schematic of the THz system based on the WVA approach. (a) Phase variation measurement system. (b) Amplitude variation measurement system.

purely real weak value derived from eq. (8). The THz wave after postselection then undergoes measurement using a THz detector to quantify amplitude variations. All experiments were conducted under standard room temperature and humidity conditions to ensure that environmental factors did not influence the results.

In the terahertz system illustrated in Figure 1b, we employed various postselected states as depicted in Figure 2a. When the terahertz polarizer P2 is oriented orthogonally to THz polarizer P1, the phase $\phi_{ ext{CEP}}$ in the initial state is $\pi/2$ (as shown in Figure 2c), where the positive and negative peak-to-peak values are nearly equal. Upon rotating the terahertz polarizer P2 by +4° around the orthogonal center, Figure 2c shows that the negative peak electric field exceeds the positive peak electric field, causing ϕ_{CEP} to shift to $\pi.$ Conversely, when P2 is rotated -4° around the orthogonal center, the direction of the electric field is reversed, resulting in ϕ_{CEP} becoming 0, as illustrated in Figure 2c. Additionally, we utilized the terahertz system depicted in Figure 1a and set different postselected states as shown in Figure 2b. Notably, due to the presence of a quarter-wave plate, a reflection peak is observed at 92 ps. Furthermore, when THz polarizer P1 and P2 are orthogonal, ϕ_{CEP} is $\pi/2$ (as shown in Figure 2d), and the peak value of the reflected signal is greater than that of ϕ_{CEP} at both 0 and π , and it also surpasses the main peak at 83 ps. When the terahertz polarizer P2 is rotated $\pm 4^{\circ}$ around the orthogonal center, the behavior is consistent with that observed in Figure 2c. Thus, the CEP shift was

effectively realized through the manipulation of terahertz polarizers P1 and P2, allowing for clear observation of the changes in the temporal waveforms of the THz pulse using this terahertz system. Figure S1 (Supplementary Materials) illustrates the terahertz time-domain electric field diagrams for the rotated QWP. Notably, compared to Figure 2, the change in electric field polarity is less pronounced when the polarizer is rotated by the same angle. The ability to manipulate terahertz waveforms is critical for a variety of applications, including terahertz scanning tunneling microscopy (THz-STM), which has traditionally employed pairs of spherical or cylindrical lenses or metamaterial arrays to achieve broadband THz CEP control [37]-[39].

We first utilized the terahertz system depicted in Figure 1a to measure the phase shift. The postselected parameters were $\kappa = 0.0349$, 0.0698, and 0.0872 rad, selected three times. Each time, THz polarizer 1 was adjusted by 0.0058 rad for $\kappa = 0.0349$ rad, and by 0.0116 rad for $\kappa =$ 0.0698 and 0.0872 rad. Figure 3a and b depicts the obtained time domain spectral change from 70 to 90 ps with an amplitude of $\kappa=\pm 0.0349\,\mathrm{rad}$, while Figure 3c and d shows the peak-to-peak value of the time domain signal. In Figure 3a and b, the 9 sampling curves of the time domain signal are spaced apart and do not overlap, even when THz polarizer 1 rotates by 0.0058 rad each time. Additionally, the THz quarter-wave plates QWP1 and QWP2 in the optical path cause multiple reflections due to incomplete parallelism, resulting in a reflection peak at 92 ps in the time

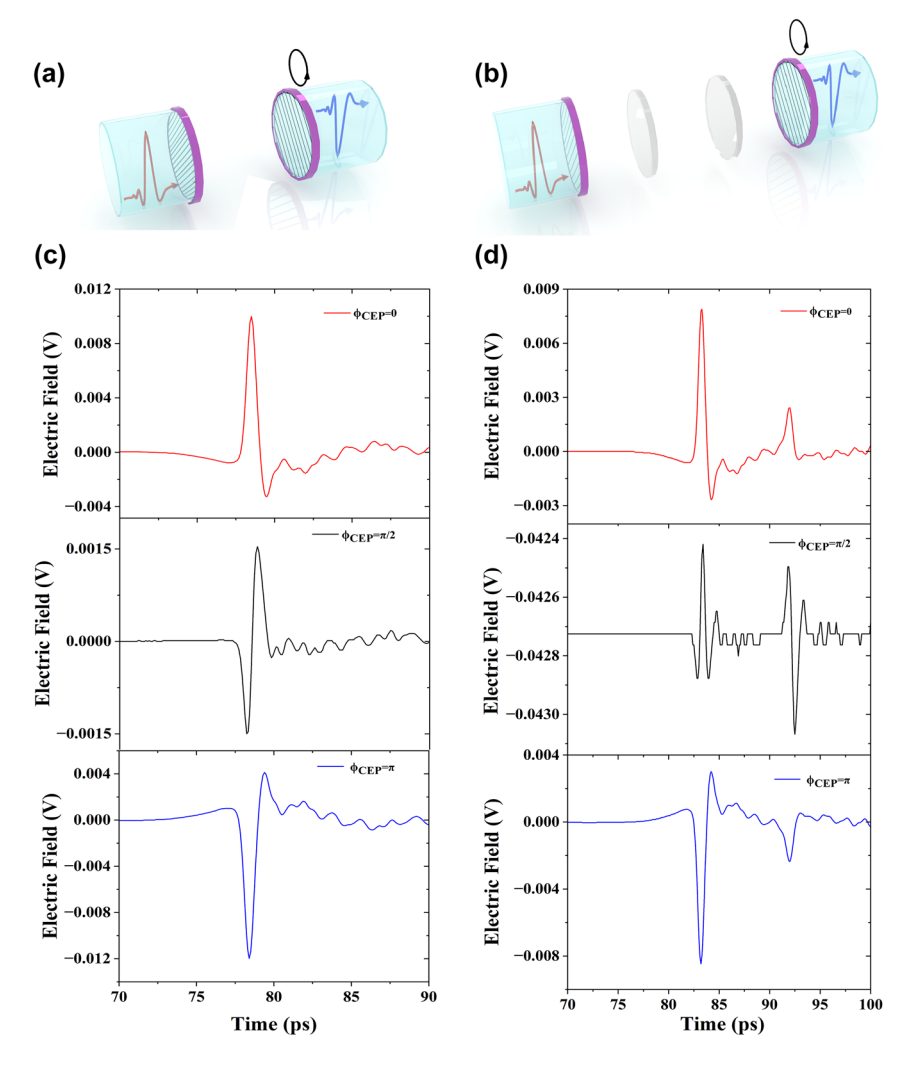


Figure 2: Different postselected states correspond to THz electric fields characterized by various CEPs of $\phi_{\text{CEP}} = 0$, $\pi/2$, and π . (a) A schematic illustration of THz polarizer 1 and polarizer 2, depicting the rotation of THz polarizer 2 to prepare different postselected states. (b) A corresponding schematic for the THz electric fields associated with $\phi_{\text{CEP}} = 0$, $\pi/2$, and π based on the configuration in part (a). (c) A schematic representation of THz polarizer 1, THz quarter-wave plates QWP1 and QWP2, along with THz polarizer 2, illustrating the rotation of THz polarizer 2 to generate different postselected states. (d) A corresponding schematic for the THz electric fields associated with $\phi_{\text{CEP}} = 0$, $\pi/2$, and π as depicted in part (c).

domain signal. Furthermore, since the electric field is a vector, adjusting THz polarizer 2 by ± 0.0349 rad after making THz polarizer 1 and THz polarizer 2 orthogonal causes the time domain signal to reverse. Figure 3c and d also show the peak-to-peak value changes linearly and in opposite directions with the continuous adjustment of THz polarizer 1. Figure 3c and d shows phase changes ranging from -0.0187 rad to 0.0183 rad, with intervals of 0.004 rad. In Figure 3a and b, the electric field magnitude is 10^{-3} V after applying pre- and postselection because the number of photons is greatly reduced. Before the pre- and postselection, the peak value of the electric field was approximately 0.35 V. The electric field strength |E| of the terahertz detector is directly proportional to the formula intensity

I, as expressed by the equation $|E| \propto I$. This relationship serves as the foundation for subsequent calculations. The sensitivity of the phase detection is calculated as $S_{\alpha} = \Delta(|E_{\alpha}^{+}| - |E_{\alpha}^{-}|)/\Delta\alpha = 0.3133 \, \text{V/rad}$, and the standard deviation of the peak-to-peak value is measured as $\sigma|E_{\alpha}| = 1.57 \times 10^{-4} \, \text{V}$, resulting in a terahertz wave phase resolution of $R_{\alpha} = \sigma|E_{\alpha}|/S_{\alpha} = 5.02 \times 10^{-4} \, \text{rad}$. The phase change, sensitivity, and resolution of the terahertz quarterwave plate are consistent starting at its 60 μ m wavelength, eliminating the need for additional phase testing at single wavelengths. Figure 3e and f presents the frequency domain spectroscopy using time domain signals for fast Fourier transform (FFT). After the FFT, it can be seen that since electric field strength |E| is a scalar, Figure 3e and f

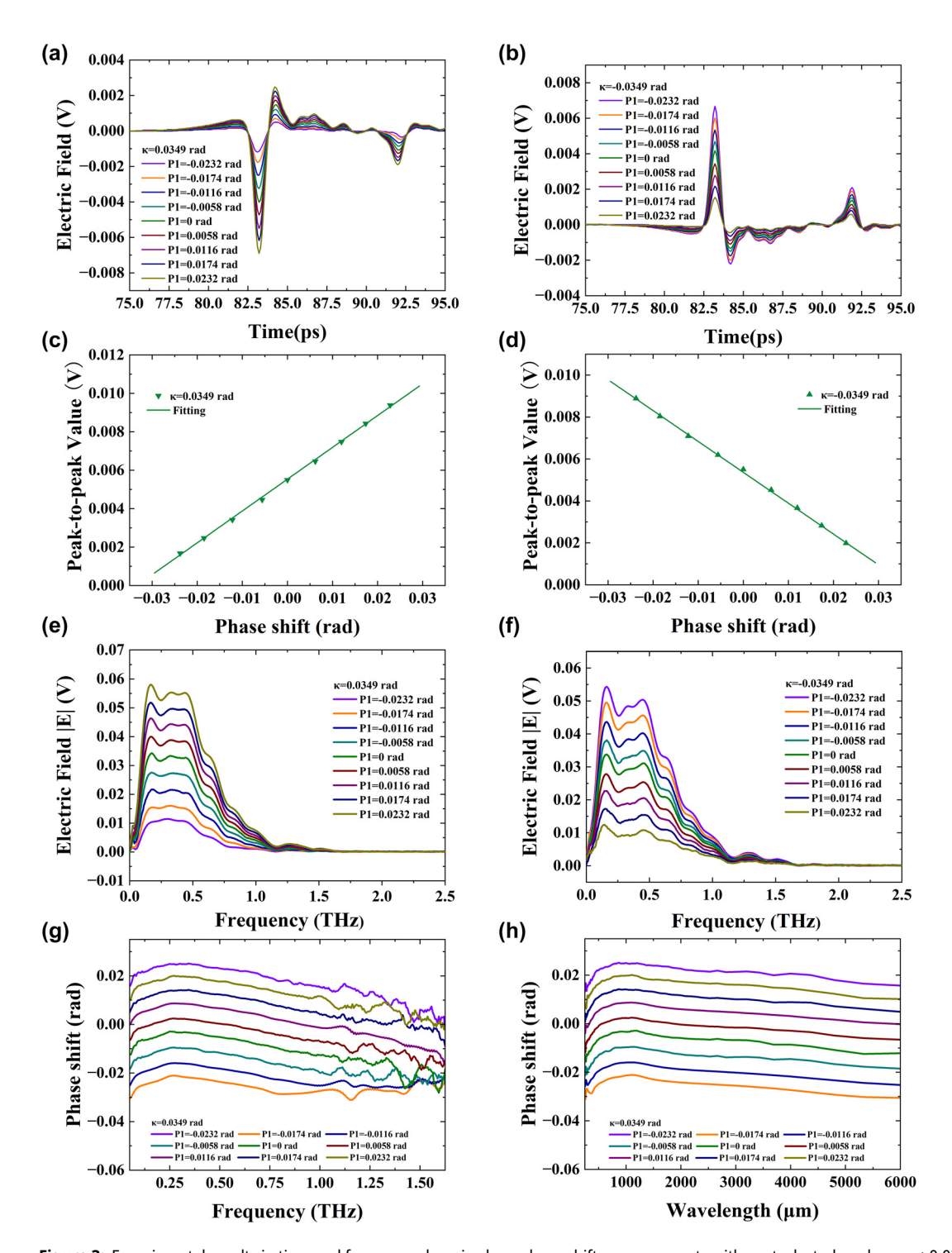


Figure 3: Experimental results in time and frequency domain show phase shift measurements with postselected angle $\kappa=\pm0.0349$ rad. (a) Electric field with $\kappa=0.0349$ rad in time domain. (b) Electric field with $\kappa=-0.0349$ rad in time domain. (c) Peak-to-peak signal with $\kappa=0.0349$ rad in time domain. (d) Peak-to-peak signal with $\kappa=-0.0349$ rad in time domain. (e) Frequency domain spectroscopy with $\kappa=0.0349$ rad. (f) Frequency domain spectroscopy with $\kappa = -0.0349$ rad. (g) Function of phase shift α and frequency. (h) Function of phase shift α and wavelength.

no longer have opposite directions except for the different order of signal size. By processing the frequency domain signal, Figure 3g and h displays the relationship between phase α and frequency with a range of 0.05–1.625 THz and wavelength with a range of 250-6,000 μm. In addition, Figure S2 (in the Supporting Information) shows the data for $\kappa = \pm 0.0698$ rad, and Figure S3 (in the Supporting Information) shows the data for $\kappa = \pm 0.0872 \, \text{rad}$, both of which are similar to Figure 3. These results indicate that the stability of our system ensures that the resolution of different postselected phases is within 10^{-4} rad. Our findings are consistent with previous studies using wide spectrum light (visible to infrared) for phase weak measurements, which also achieved a resolution of 10 ⁻⁴ rad [40], [41]. In contrast, Qiu et al. employed a monochromatic laser (He-Ne laser) and achieved phase delay estimation with a precision on the order of 10^{-5} rad [42]. This enhancement in precision can be attributed to the dispersion effects produced by broad spectrum light sources, which are significant factors limiting measurement accuracy in high-precision optical systems. Furthermore, the extinction ratio of our THz polarizer is greater than 1,000:1, whereas the Glan-Taylor polarizer employed in measurements using a monochromatic light source boasts an extinction ratio of 100,000:1. This disparity in extinction ratios further contributes to reduced measurement accuracy in our setup.

Next, we employed the terahertz system shown in Figure 1b to measure the amplitude shift. Interestingly, the experimental results were similar to those obtained using the setup in Figure 1a. The postselected parameters included $\chi = 0.0349$, 0.0698, and 0.0872 rad, which were selected three different times. Each time, THz polarizer 1 was finetuned by 0.0058 rad when $\chi = 0.0349$ rad, and by 0.0116 rad when $\gamma = 0.0698$ and 0.0872 rad. Figure 4a and b illustrates the change in the time domain with an amplitude of $\gamma =$ ±0.0349 rad, and Figure 4c and d shows the peak-to-peak value of the time domain signal. In Figure 4a and b, the 9 sampling signal curves of the time domain signal are spaced apart and do not overlap, even when THz polarizer 1 rotates by 0.0058 rad each time. Additionally, the THz quarter-wave plates OWP1 and OWP2 are not in the optical path so that no multiple reflections due to incomplete parallelism results, thus no reflection peak appear at 92 ps in the time domain signal. Furthermore, same as in the previous analysis, since the electric field is a vector, adjusting THz polarizer 2 by ± 0.0349 rad after making THz polarizer 1 and THz polarizer 2 orthogonal causes the time domain signal to reverse. Figure 4c and d also show that the peak-to-peak value changes linearly and in opposite directions with the continuous adjustment of THz polarizer 1. Figure 4c and d shows amplitude changes ranging from -0.0238 rad to 0.0228 rad, with intervals of 0.0056 rad. Using the formula, the sensitivity of the amplitude is calculated $S_{\beta} = \Delta \left(\left| E_{\beta}^{+} \right| - \left| E_{\beta}^{-} \right| \right) / \Delta \beta = 0.4351 \text{ V/rad, and the}$ standard deviation of the peak-to-peak value is measured as $\sigma |E_{\beta}| = 1.9 \times 10^{-4}$ V, resulting in a terahertz wave amplitude resolution of $R_{\beta} = \sigma |E_{\beta}|/S_{\beta} = 4.38 \times 10^{-4} \text{ rad.}$ The amplitude change, sensitivity, and resolution of the terahertz are consistent starting at its 60 µm wavelength, eliminating the need for additional amplitude testing at single wavelengths. Figure 4e and f presents the frequency domain spectroscopy using time domain signals for FFT. After FFT transformation, it can be seen that since electric field strength |E| is a scalar, Figure 4e and f no longer have opposite directions except for the different order of signal size. By processing the frequency domain signal, Figure 4g and h displays the relationship between amplitude shift β and frequency with a range of 0.05-1.625 THz and wavelength with a range of 250-6,000 μm. In addition, Figure S4 (in the Supporting Information) shows the data for $\gamma =$ ±0.0698 rad, and Figure S5 (in the Supporting Information) shows the data for $\chi = \pm 0.0872$ rad, both of which are similar to Figure 4. These results also indicate that the stability of our system ensures that the resolution of different postselected amplitude is within 10^{-4} rad. It is important to note that the resolution of phase and amplitude measurements can be significantly affected by various sources of noise, primarily arising from the terahertz transmitter, delay line, terahertz detector, incident angle error of the terahertz wave, and fluctuations in the experimental environment. For instance, environmental factors such as temperature and humidity can impact the stability of terahertz signals, leading to additional noise. To minimize measurement errors, we have taken several steps in our experimental design. Specifically, the spectrum for each measurement is determined by averaging the results of three independent experiments. Each data collection consists of averaging 60,000 individual spectra collected over a 60-s timeframe. This approach helps to enhance the reliability and accuracy of our measurements by effectively reducing the impact of random noise from various sources.

The postselection parameter $\kappa \ll 1$ or $\chi \ll 1$ is fixed, although the THz wave electric field or intensity caused by phase or amplitude shift undergoes weak value amplification $\left(\left|A_{w(\alpha),(\beta)}^{\pm}\right|\right)$, the overall attenuation of the THz wave electric field or intensity $(\sin^2 \kappa \text{ or } \sin^2 \chi)$ leads to a general decrease in THz wave electric field or intensity $(\sin^2 \kappa \left| A^{\pm}_{w(\beta)} \right| \approx \sin \kappa \text{ or } \sin^2 \chi \left| A^{\pm}_{w(\alpha)} \right| \approx \sin \chi$). So, how is the effect of linear weak value amplification manifested? To elucidate this point intuitively, we introduce the contrast ratio $\eta_{\alpha,\beta} = \left(\left|E_{\alpha,\beta}^{+}\right| - \left|E_{\alpha,\beta}^{-}\right|\right) / \left(\left(\left|E_{\alpha,\beta}^{+}\right| + \left|E_{\alpha,\beta}^{-}\right|\right) / 2\right)$. From Figure 5a and b, we can see that as the postselection parameter decreases, the contrast ratio between phase and amplitude $\eta_{lpha,eta}$ increases. The contrast ratio $\eta_{lpha,eta}$ is proportional to the weak value $A^{\pm}_{w(\alpha),(\beta)}$, where the case $\left|A^{\pm}_{w(\alpha),(\beta)}\right| =$

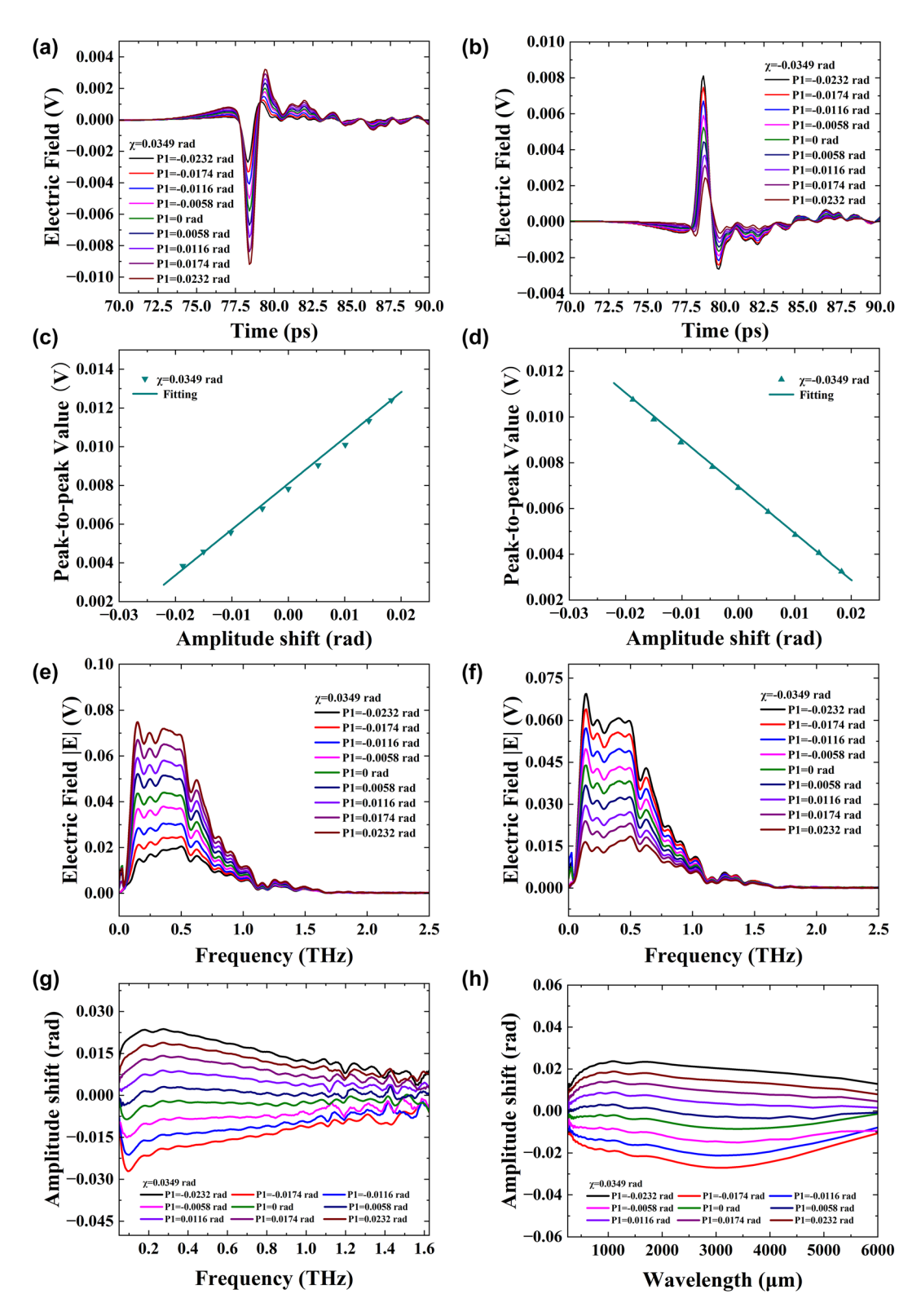


Figure 4: Experimental results in time and frequency domains show amplitude shift measurements with postselected angle $\chi = \pm 0.0349$ rad. (a) Electric field with $\chi=0.0349$ rad in time domain. (b) Electric field with $\chi=-0.0349$ rad in time domain. (c) Peak-to-peak signal with $\chi=0.0349$ rad in time domain. (d) Peak-to-peak signal with $\chi = -0.0349$ rad in time domain. (e) Frequency domain spectroscopy with $\chi = 0.0349$ rad. (f) Frequency domain spectroscopy with $\chi=-0.0349$ rad. (g) Function of amplitude shift eta and frequency. (h) Function of amplitude shift eta and wavelength.

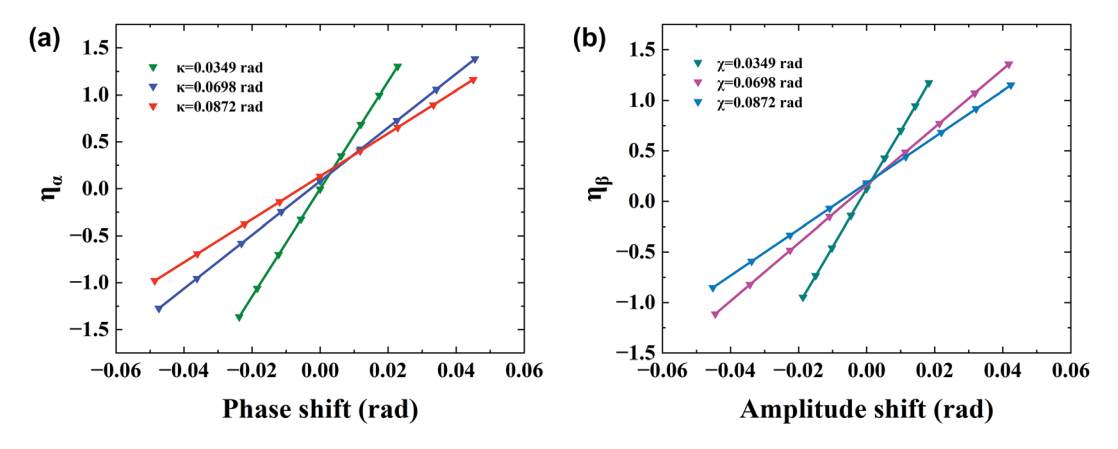


Figure 5: The contrast ratio $\eta_{\alpha,\beta}$ of different postselection parameters. (a) The contrast ratio η_{α} of the phase shift with different $\kappa = 0.0349$, 0.0698, and 0.0872 rad, respectively. (b) The contrast ratio η_B of the phase shift with different $\chi=0.0349, 0.0698$, and 0.0872 rad, respectively.

cot(0.0349) represents the maximum slope for phase and amplitude shifts.

Based on the experimental data, we found that, within a certain range, a smaller postselection angle corresponds to a larger weak value. However, it is not the case that a smaller postselection angle will always result in greater magnification. For instance, Oiu et al. discovered that when postselection angles approach complete orthogonality to preselection [42], there is a maximum weak value, after which magnification decreases rapidly as the postselection angle continues to decrease.

Ding et al. previously developed dual-wavelength metasurfaces capable of independently controlling both phase and amplitude at specific terahertz wavelengths. However, this design suffers from significant wavelength dependence, which limits its effectiveness across a broader range of wavelengths. Additionally, the complexity of the design and manufacturing processes necessitates parameter adjustments meticulous and extensive simulations [43]. In contrast, Kakenov et al. utilized graphene in electrolyte-gated devices to modulate terahertz phase and amplitude. The performance of these devices is heavily influenced by the quality and consistency of the graphene used. Furthermore, electrolyte gating introduces potential stability issues, as these devices can be sensitive to environmental factors such as humidity and temperature. Achieving the necessary charge density for effective electrolyte gate control poses challenges due to the intricate nature of the manufacturing processes. Moreover, scaling production and integrating these technologies cost-effectively present significant hurdles, given the precision required in manufacturing [44]. In our experiment, we demonstrate a method applicable across a wide bandwidth, rather than being limited to a single wavelength, while effectively modulating both phase and amplitude. This approach avoids the need for complex structures, ensuring repeatability and stability. Notably, without additional control conditions, the modulation resolution for both phase and amplitude can reach 10^{-4} rad, which is significantly finer than the phase range $(-\pi$ to π) and amplitude range (0-1) achieved in the previously discussed methods.

To verify the theory and the polarization-sensitive phase and amplitude THz measurement system, we used chiral samples in the next phase of our experiments. Chirality, the property of molecular asymmetry where molecules cannot be superimposed onto their mirror images, is prevalent in nature [45], [46]. Chiral molecules exhibit different biochemical behaviors from their mirror images, making them crucial in various biological processes. When a linearly polarized light beam passes through a chiral sample, it exhibits optical activity (OA), which comprises ORD and CD. OA refers to the interaction of chiral enantiomers with polarized light, evident in CD and ORD. CD measures the differential absorption of left (LCP) and right (RCP) circularly polarized light, corresponding to phase variation. ORD, on the other hand, measures the differential refraction, corresponding to amplitude variation. The spectra of both CD and ORD differentiate enantiomers by their sign and can be linked to absolute molecular configurations. Such interactions can be exploited as powerful tools for detecting chiral molecules, known as chiral sensing. Optical chiral sensing is advantageous because it is easy to implement and noninvasive to analytes. However, it presents challenges due to the extremely weak chiroptical signals of natural molecules $(10^{-4} - 10^{-6})$ that of optical absorption), and that such weak signals coexist with much stronger signals of achiral absorptions.

CD and ORD correspond to the imaginary and real parts of the complex chiral susceptibility, much like how ordinary absorption and dispersion correspond to the imaginary and real parts of the complex refractive index [8]. To characterize both the imaginary (CD) and real (ORD) parts of the chiroptical susceptibility simultaneously, we will use our THZ-VWA system to construct an imaginary weak value and a real weak value.

Figure 6 depicts the scenario when linearly polarized terahertz light (an equal superposition of left circularly polarized (LCP) and right circularly polarized (RCP) light) passes through a sample with opposite chiral properties [6]. The THz-ORD and THz-CD signals arise due to differences in the refractive index and absorption coefficient. After the light interacts with the two different enantiomers, the (R)form (purple) and the (S)-form (blue), these perpendicular components are out of phase with each other. If the change is small, the individual THz-CD (solid line) and THz-ORD (dashed line) components are approximately orthogonal.

The polarization state of THz wave is preselected as follows

$$\left|\psi_{\text{pre}}\right\rangle = \frac{1}{\sqrt{2}}(|H\rangle + |V\rangle) = \frac{1}{2}((1-i)|L\rangle + (1+i)|R\rangle),\tag{10}$$

where

$$|L\rangle = \frac{1}{\sqrt{2}}(|H\rangle + i|V\rangle),$$
 (11)

$$|R\rangle = \frac{1}{\sqrt{2}}(|H\rangle - i|V\rangle),$$
 (12)

where, we decompose the $\pi/4$ linearly polarized light into left-handed and right-handed circularly polarized light with equal amplitudes. $|L\rangle$ and $|R\rangle$ represent the states of lefthanded circularly polarized light and right-handed circularly polarized light, respectively. And as before, $|H\rangle$ and $|V\rangle$ denote the horizontal and vertical polarization states, respectively.

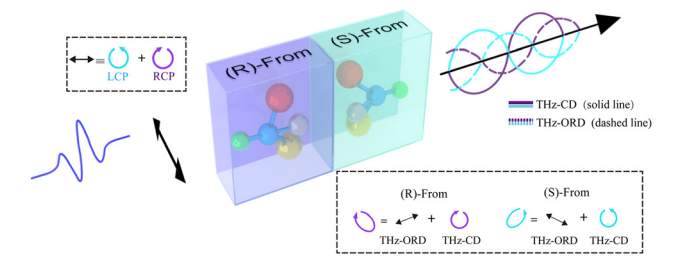


Figure 6: Simplified diagram of the basic principle of THz-ORD and THz-CD measurements includes the process of changing the polarization state. The THz wave is linearly polarized before interacting with a chiral sample. THz-ORD describes the difference in the propagation speeds of left- and right-circularly polarized light, whereas THz-CD refers to the difference in light absorption between these two polarizations.

When a linearly polarized THz wave passes through chiral molecules, differences in refractive index and absorption coefficient introduce small phase and amplitude changes between the left-handed and right-handed circularly polarized components. These changes are known as ORD and CD signals, respectively. ORD causes an amplitude shift in the beam, while CD causes a phase change. Therefore, the operators for measuring amplitude and phase can be used to describe the operators for ORD and CD.

$$\widehat{U} = \exp\left(\frac{\theta(\lambda) + i\delta(\lambda)}{2}\widehat{A}\right),\tag{13}$$

where, the ORD and CD signals of the sample are represented by the following equations:

$$\theta(\lambda) = \frac{2\pi l(n_L - n_R)}{\lambda},\tag{14}$$

$$\delta(\lambda) = \frac{\ln(10)(\varepsilon_L - \varepsilon_R)Cl}{2},\tag{15}$$

in these equations, $\varepsilon_{\mathit{L(R)}}$ represents the molar extinction coefficient, $n_{L(R)}$ represents the refractive index, λ represents the wavelength, C represents the concentration, and lrepresents the optical path length. Also, $\widehat{A} = |L\rangle\langle L| - |R\rangle\langle R|$ is the observable quantity of the two-level quantum system.

After the beam passes through the chiral sample, the state of the system changes to

$$|\psi'\rangle = \widehat{U}|\psi_{\text{pre}}\rangle$$

$$= \exp\left(\frac{\theta(\lambda) + i\delta(\lambda)}{2}\widehat{A}\right)\frac{1}{2}((1-i)|L\rangle + (1+i)|R\rangle)$$

$$= \frac{1}{2}\left(\exp\left(\frac{\theta(\lambda) + i\delta(\lambda)}{2}\right)(1-i)|L\rangle + \exp\left(-\frac{\theta(\lambda) + i\delta(\lambda)}{2}\right)(1+i)|R\rangle\right), \quad (16)$$

in the weak measurement model, $\theta(\lambda) \ll 1$ and $\delta(\lambda) \ll 1$.

Subsequently, the ORD signal is measured by constructing a postselected polarization state with a real weak value, similar to the amplitude measurement above

$$\left|\psi_{\text{post}(\theta(\lambda))}^{\pm}\right\rangle = \cos\left(\frac{\pi}{4} \mp \chi\right)|L\rangle - \sin\left(\frac{\pi}{4} \mp \chi\right)|R\rangle.$$
 (17)

According to the general expression for the weak value, the real weak value is derived from the preselected and postselected states

$$A_{w(\theta(\lambda))}^{\pm} = \frac{\left\langle \psi_{\text{post}(\theta(\lambda))}^{\pm} \middle| \widehat{A} \middle| \psi_{\text{pre}} \right\rangle}{\left\langle \psi_{f(\theta(\lambda))}^{\pm} \middle| \psi_{\text{pre}} \right\rangle} = \pm \cot \chi. \tag{18}$$

The intensity of the postselected THz wave corresponding to the state is given by

$$I_{\theta(\lambda)}^{\pm} = I_{0} \left| \left\langle \psi_{\text{post}(\theta(\lambda))}^{\pm} \middle| \exp\left(\frac{\theta(\lambda) + i\delta(\lambda)}{2} \widehat{A}\right) \middle| \psi_{\text{pre}} \right\rangle \right|^{2}$$

$$\approx I_{0} \left| \left\langle \psi_{\text{post}(\theta(\lambda))}^{\pm} \middle| \psi_{\text{pre}} \right\rangle \right|^{2} \left[1 + \theta(\lambda) \operatorname{Re}\left(A_{w(\theta(\lambda))}^{\pm}\right) \right]$$

$$= I_{0} \sin^{2} \chi \left[1 + \theta(\lambda) \operatorname{Re}\left(A_{w(\theta(\lambda))}^{\pm}\right) \right], \tag{19}$$

Here, I_0 denotes the initial THz intensity before postselection. In eq. (19), the approximation is based on the condition that $\left|A_{w(\theta(\lambda))}^{\pm}\right|^2 \left(\delta(\lambda)^2 + \theta(\lambda)^2\right)/4 \ll 1$ and $\chi \ll 1$.

Then, the CD signal is measured by constructing a postselected polarization state with an imaginary weak value

$$\left| \psi_{\text{post}(\delta(\lambda))}^{\pm} \right\rangle = \frac{1}{\sqrt{2}} \left[\exp(\mp i\kappa) |L\rangle - \exp(\pm i\kappa) |R\rangle \right], \quad (20)$$

 \pm represents two symmetric postselection states. According to the weak value calculation formula, the imaginary weak value is derived from the preselected and postselected states

$$A_{w(\delta(\lambda))}^{\pm} = \frac{\left\langle \psi_{\text{post}(\delta(\lambda))}^{\pm} \middle| \widehat{A} \middle| \psi_{\text{pre}} \right\rangle}{\left\langle \psi_{\text{post}(\delta(\lambda))}^{\pm} \middle| \psi_{\text{pre}} \right\rangle} = \mp i \cot \kappa.$$
 (21)

The intensity of the postselected THz wave corresponding to the state is given by

$$I_{\delta(\lambda)}^{\pm} = I_{0} \left| \left\langle \psi_{\text{post}(\delta(\lambda))}^{\pm} \middle| \exp\left(\frac{\theta(\lambda) + i\delta(\lambda)}{2} \hat{A}\right) \middle| \psi_{\text{pre}} \right\rangle \right|^{2}$$

$$\approx I_{0} \left| \left\langle \psi_{\text{post}(\delta(\lambda))}^{\pm} \middle| \psi_{\text{pre}} \right\rangle \right|^{2} \left[1 - \delta(\lambda) \operatorname{Im}\left(A_{w(\delta(\lambda))}^{\pm}\right) \right]$$

$$= I_{0} \sin^{2} \kappa \left[1 - \delta(\lambda) \operatorname{Im}\left(A_{w(\delta(\lambda))}^{\pm}\right) \right], \tag{22}$$

Here, I_0 denotes the initial THz intensity before postselection. In eq. (22), the approximation is based on the condition that $\left|A_{w(\delta(\lambda))}^{\pm}\right|^2 \left(\delta(\lambda)^2 + \theta(\lambda)^2\right)/4 \ll 1$, $\kappa \ll 1$.

We first utilized the THz-WVA system to measure the THz-ORD spectra of (R)- and (S)-limonene at $\delta(\lambda)=0$, with postselected parameters $\chi=0.0349\,\mathrm{rad}$ (in Figure 5, the postselected parameter $\chi=0.0349\,\mathrm{rad}$ is the largest weak value). The (R)- and (S)-limonene (C₁₀H₁₆) employed in the experiment are both PYRAM brand products, each with a purity exceeding 95 % and a molecular weight of 136.23 g/mol. Both limonenes are in liquid form and were sourced from Shanghai Bohu Biotechnology Co., Ltd. The sample cell's window material is TPX, sourced from Dongguan Daehan Polymer Plastic Co., Ltd, China, with a diameter of 40 mm and a thickness of 2 mm. The gasket, with

an inner diameter of 35 mm, an outer diameter of 39 mm, and a thickness of 2.5 mm, provides an optical path length of 2.5 mm for the (R)- and (S)-limonene samples. Figure 7a and b shows time domain changes from 0 to 160 ps with an amplitude of $\gamma = \pm 0.0349$ rad, while Figure 7c and d shows the frequency domain signal after performing FFT on the time domain signal. Figure 7a and b reveals that after adding 2.3 mL of (R)- and (S)-limonene, there is a time delay compared to the empty sample cell. Since (R)- and (S)-limonene are equal in volume, their signals overlap in the time domain. As before, since the electric field is a vector, adjusting THz polarizer 2 by ±0.0349 rad after making THz polarizer 1 and THz polarizer 2 orthogonal causes the time domain signal to reverse. Additionally, the time domain peak-to-peak values of (R)- and (S)-limonene differ due to their different terahertz absorption coefficients and refractive indices for left and right circularly polarized light. The change in optical rotation electric field |E|for (R)-limonene is 7.05×10^{-5} V and for (S)-limonene is -3.25×10^{-5} V, indicating that the optical rotation directions of (R)- and (S)-limonene are opposite. Clearly, the change in electric field |E| due to absorption is much greater than that due to optical rotation. This discrepancy explains why traditional terahertz systems cannot directly measure chiral samples. However, weak value amplification can amplify weak signals by several orders of magnitude while simultaneously suppressing technical noise to an extremely low level. This enhancement improves measurement resolution, enabling the effective measurement of chiral samples. Figure 7c and d presents the frequency domain spectra after FFT of the time domain signals. Processing the frequency domain signal, Figure 7e displays the THz-ORD spectra of (R)- and (S)-limonene, showing the relationship between $\theta(\lambda)$ and frequency from 0.1 to 0.7 THz, with (R)and (S)-limonene ORD components being approximately orthogonal.

We then utilized the THZ-WVA system to measure the THz-CD spectra of (R)- and (S)-limonene at $\theta(\lambda)=0$, with postselected parameters $\kappa=0.0349$ rad. Figure 8a and b shows time domain changes from 0 to 160 ps with an amplitude of $\kappa=\pm0.0349$ rad, while Figure 8c and d displays the frequency domain signal after performing FFT on the time domain signal. Figure 8a and b reveals that after adding 2.3 mL of (R)- and (S)-limonene, there is a time delay compared to the empty sample cell. Since (R)- and (S)-limonene are equal in volume, their signals overlap in the time domain. Additionally, the time domain peak-to-peak values of (R)- and (S)-limonene differ due to their different terahertz absorption coefficients and absorption of left and right circularly polarized light. Processing the frequency domain

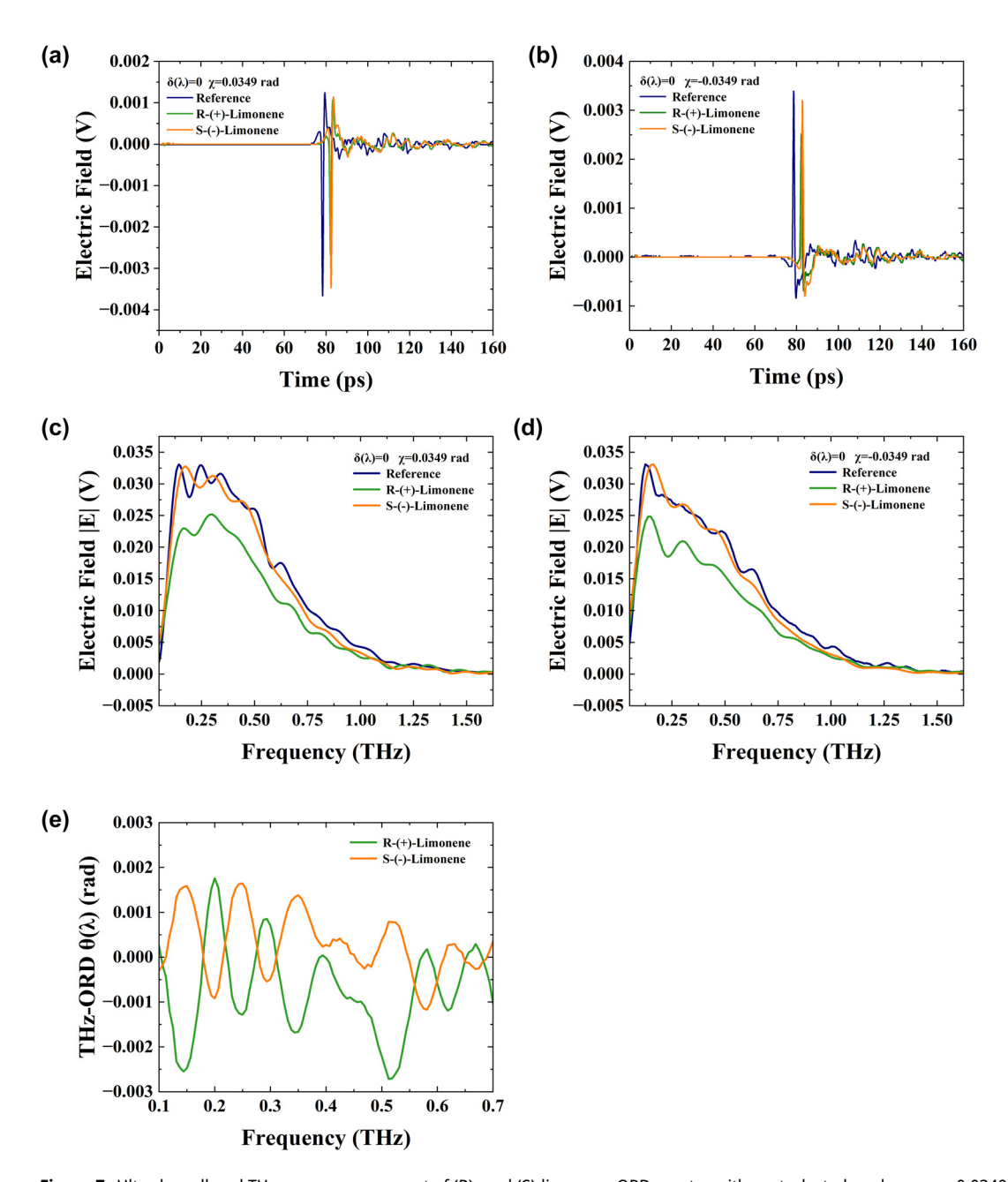


Figure 7: Ultra-broadband THz wave measurement of (R)- and (S)-limonene ORD spectra with postselected angles $\chi=\pm 0.0349$ rad. (a) The time-domain electric field corresponding to $\chi=0.0349$ rad. (b) The time-domain electric field corresponding to $\chi=-0.0349$ rad. (c) Frequency domain spectroscopy for $\chi=0.0349$ rad. (d) Frequency domain spectroscopy for $\chi=-0.0349$ rad. (e) (R)-limonene absorption spectra. (f) (S)-limonene absorption spectra.

signal, Figure 8e displays the THz-CD spectra of (R)- and (S)-limonene, showing the relationship between $\delta(\lambda)$ and frequency from 0.1 to 1.125 THz, with the THz-CD components of (R)- and (S)-limonene being approximately orthogonal. It can be seen that the THz-CD spectrum of (R)-limonene has some data in the order of magnitude of 10^{-5} rad, which

further explains why traditional terahertz methods cannot directly measure the THz-CD signal.

Since ${\rm CCl_4}$ as solvent for limonene is toxic that our laboratory is not ventilated to handle, we did not conduct tests on different concentrations of (R)- and (S)-limonene as of this writing.

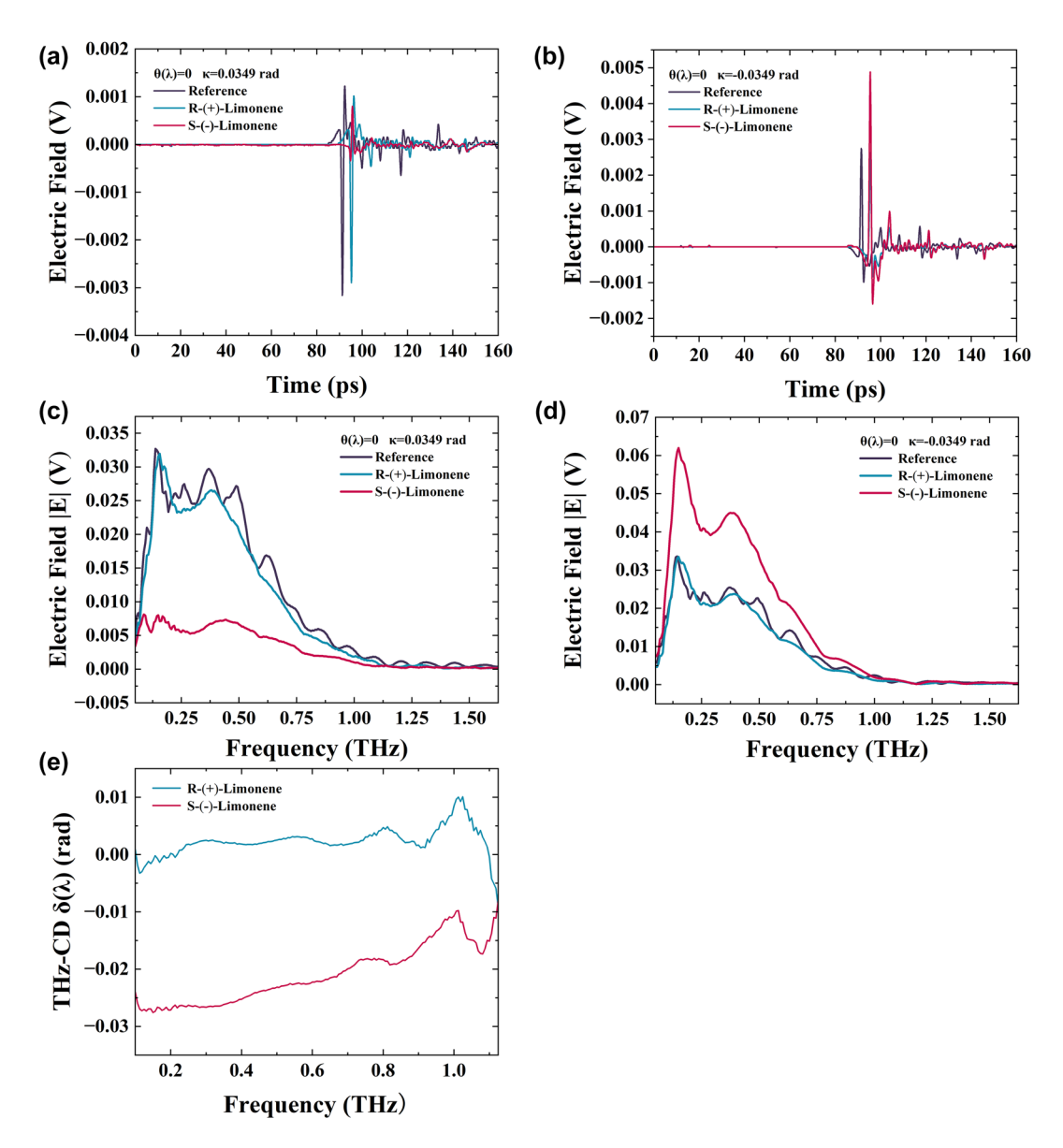


Figure 8: Ultra-broadband THz wave measurement of (R)- and (S)-limonene CD spectra with postselected angles $\kappa = \pm 0.0349$ rad. (a) The time-domain electric field corresponding to $\kappa = 0.0349$ rad. (b) The time-domain electric field corresponding to $\kappa = -0.0349$ rad. (c) Frequency domain spectroscopy for $\kappa = 0.0349$ rad. (d) Frequency domain spectroscopy for $\kappa = -0.0349$ rad. (e) (R)- and (S)-limonene THz-CD spectra.

We also utilized this THz system to test D(+)-lactose (C₁₂H₂₂O₁₁), which was sourced from Shanghai Yuanye Biotechnology Co., Ltd., with a purity exceeding 98 %. No further purification was performed prior to its use. D(+)lactose and polyethylene were thoroughly ground and mixed in weight ratios of 30 %, 50 %, and 70 %, resulting in a total mass of 150 mg. A slicer was employed to apply a pressure of 12 tons/cm² for 2 min, yielding slices with a diameter of 13 mm and a thickness ranging from 1 to 1.3 mm. Measurements were conducted using the optical path depicted in Figure 1. Figure 9a and b illustrates the absorption coefficient of lactose. Notably, under the same postselection

conditions, the absorption coefficient increases with mass fraction, with the 70 % lactose sample exhibiting the highest absorption coefficient. In the absence of weak measurement techniques, the peak of the original time-domain signal exceeded that of the lower portion, with the absorption peak for 70 % lactose recorded at 0.53 THz and 20 cm⁻¹. Upon reversing the electric field in the time domain when $\phi_{\text{CEP}} = 0$ (as seen in Figure 2c), the absorption coefficient of 70 % lactose reached 50 cm⁻¹ at 0.53 THz, reflecting a 150 % increase compared to the original value, as shown in Figure 9a. Conversely, when $\phi_{\text{CEP}} = 0$ (Figure 2d), the absorption coefficient of 70 % lactose reached 45 cm⁻¹ at 0.53 THz, indicating

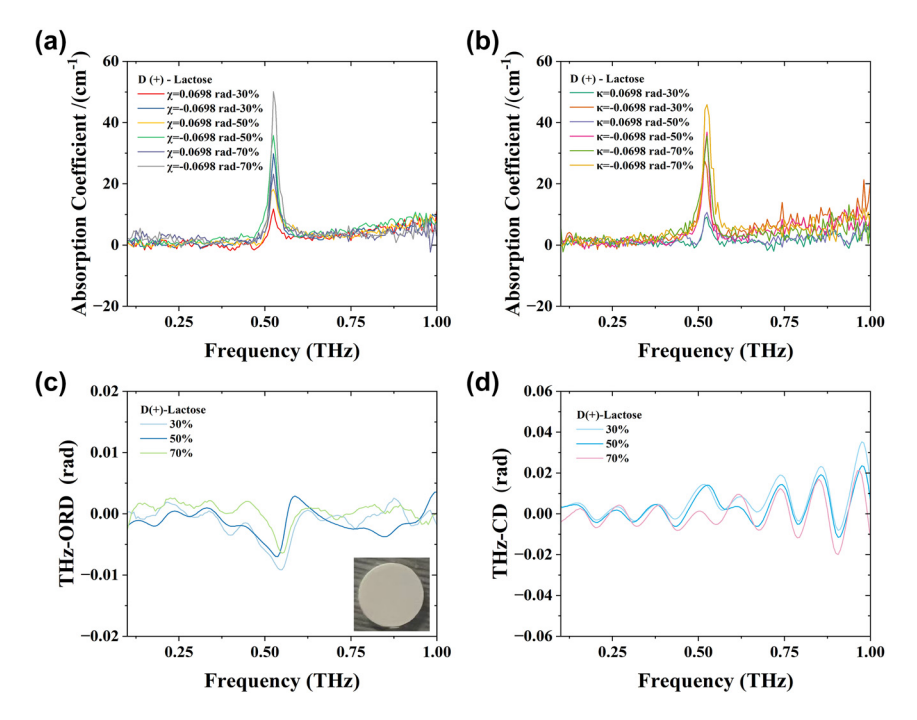


Figure 9: THz spectroscopic analysis of D(+)-lactose tablets. (a) D(+)-lactose absorption coefficient of 30 %, 50 %, and 70 % when $\chi=\pm0.0698$ rad; inset shows an optical image of a sample tablet. (b) D(+)-lactose absorption coefficient of 30 %, 50 %, and 70 % when $\kappa=\pm0.0698$ rad. (c) D(+)-lactose THz-ORD spectra. (d) D(+)-lactose THz-CD spectra.

a 125 % increase compared to the original value, as shown in Figure 9b. The most significant absorption coefficient for 70 % lactose was observed when $\chi=-0.0698$ rad and $\kappa=-0.0698$ rad, while enhancements were less pronounced at $\chi=0.0698$ rad or $\kappa=0.0698$ rad.

The absorption coefficient of lactose is significantly influenced by the direction of the terahertz electric field, which can be attributed to several interrelated factors. First, the direction of the electric field alters the polarization degree of the lactose molecules, thereby affecting their response to the field. Second, the direction of the electric field determines the orientation of the molecules in space, and this orientation can influence the interactions between molecules. When the direction of the electric field changes, the resonance conditions of lactose may also shift, potentially leading to changes in the position and intensity of the absorption peaks. Additionally, the direction of the electric field affects the electronic charge distribution within the molecules, further altering their absorption characteristics. In summary, these factors interact with one another, resulting in a significant impact of the direction of the terahertz electric field on the absorption coefficient of lactose. Additionally, the absorption peak obtained without the addition of a quarter-wave plate in the postselection

process (as illustrated in Figure 9a) was higher, characterized by a smooth waveform and a prominent peak. These observations suggest that the absorption peak of lactose is influenced not only by its mass, moisture content, and temperature [47] but also by the orientation of the terahertz electric field. Figure 9c and d presents the spectrum and circular dichroism analysis of lactose, respectively. In future experiments, we plan to include an additional set of lenses to focus the THz beam onto the sample tablet for testing and comparison.

To aid the evaluation of sensor performance in this study, we compared it with representative studies on chiral sensing as summarized in Table 1. Our approach involves an optical path with two polarizers for measuring chiral liquids, contrasting with methods utilizing metal metamaterial structures, which we did not employ. It is noteworthy that large chiral nanostructures may potentially obscure molecular chiral signals, thus limiting their practical application prospect [48]. Additionally, metamaterials, once designed, are not easily modifiable, and their preparation is complex. Despite their ability to amplify signals such as CD and ORD by several orders of magnitude, they also introduce noise. Even after removing background signals, the obtained chiral sample signal often deviates significantly from the true value. This is because chiral light effects (CD and ORD) are

Table 1: Performance parameter comparison for recently reported chiral sensing.

Sensor type	Characterization parameter and signal range	Analyte	Chiral sample state	Operation mode	Ref.
Pancharatnam – Berry metasurface	Circular dichroism (—11.6° to 16.4°)	Tyrosine	Tablet	Transmission	[49]
Chiral metamaterials	Circular dichroism (—40° to 40°)	Cyclotyrosine	Biocrystals	Transmission	[50]
Metal metasurface	Circular dichroism (—45° to 45°) and optical rotatory dispersion (90° to 90°)	Amino acids	Liquid	Reflection	[5]
THz-WVA	Circular dichroism (—0.02 to 0.04 rad) and optical rotatory dispersion (—0.01 to 0.003 rad)	Limonene, lactose	Liquid, tablet	Transmission	This work

very weak, typically only 10^{-6} to 10^{-4} of the nonchiral background absorption signal.

4 Conclusions

In summary, we have presented a novel setup for THz broadband measurements of phase and amplitude variations in both the time and frequency domains using weak value amplification. Through tailored postselection parameters, we employed real weak values to precisely measure amplitude shifts. Furthermore, by integrating a THz guarter-wave plate into the setup, we effectively enlarged the postselection parameters space and were able to utilize imaginary weak values to accurately measure phase shifts. This enables us to deduce the complete polarization state variation of THz waves using the novel WVA scheme. Our method achieves a resolution of approximately 10⁻⁴ rad for both phase and amplitude variations in the time domain using the peak-to-peak value and determines phase and amplitude variations with frequency and wavelength in the frequency domain through the electric field |E| spectrum. Furthermore, we successfully detected small signals of large-volume (R)- and (S)-limonene and D(+)lactose through CD and ORD, overcoming the significant limitation of traditional THz system, which cannot directly measure the chiral optical activity of liquids and tablets. At the same time, effective manipulation of CEP offset was achieved in terahertz polarizers P1 and P2. When $\phi_{\text{CEP}} = 0$, using weak measurement techniques can greatly enhance the absorption coefficient of lactose. It was found that the absorption coefficient of lactose is influenced not only by concentration, temperature, and water content but also by the orientation of the terahertz electric field. Given its general applicability, our approach to measuring broadband THz polarization phase and amplitude and optical activity offers simplicity, affordability, and robustness, enabling a wide range of experiments beyond research laboratories.

Research funding: National Natural Science Foundation of China (Project Number: 62475276), the Sichuan Provincial Natural Science Foundation (Project Number: 2023NSFSC1389), the Major Instrumentation Development Program of the Chinese Academy of Sciences (Project Number: ZDKYYQ20220008), and the Chengdu University of Technology Graduate Quality Engineering Project (Project Number: 2022YIG030).

Author contributions: LX: methodology, investigation, data curation, writing - original draft. JX, XY, RZ, GW, LW, XL, ZL, WL, DW, and XL: investigation, data validation. TC: supervision, project administration. H-LC: writing - review & editing, project administration. All authors have accepted responsibility for the entire content of this manuscript and consented to its submission to the journal, reviewed all the results and approved the final version of the manuscript.

Conflict of interest: Authors state no conflict of interest. Informed consent: Informed consent was obtained from all individuals participating in this study.

Ethical approval: The research conducted is not related to the use of humans or animals.

Data availability: The data underlying the results presented in this paper are not publicly available at this time but may be obtained from the authors upon reasonable request.

References

- [1] H.-J. Zhao, F. Fan, T.-R. Zhang, Y.-Y. Ji, and S.-J. Chang, "Dynamic terahertz anisotropy and chirality enhancement in liquid-crystal anisotropic dielectric metasurfaces," Photonics Res., vol. 10, no. 4, pp. 1097-1106, 2022.
- [2] A. Tomasino, et al., "Solid-state-biased coherent detection of ultra-broadband terahertz pulses," Optica, vol. 4, no. 11, pp. 1358-1362, 2017.
- C. Wang, Y. Huang, R. Zhou, L. Xie, and Y. Ying, "Rapid analysis of a doxycycline hydrochloride solution by metallic mesh device-based reflection terahertz spectroscopy," Opt. Express, vol. 28, no. 8, pp. 12001-12010, 2020.

- [4] L. Luo, et al., "Simultaneously precise estimations of phase and amplitude variations based on weak-value amplification," Appl. Phys. Lett., vol. 114, no. 11, 2019. https://doi.org/10.1063/1.5083995.
- [5] Z. Zhang, C. Zhong, F. Fan, G. Liu, and S. Chang, "Terahertz polarization and chirality sensing for amino acid solution based on chiral metasurface sensor," Sens. Actuators B: Chem., vol. 330,
- [6] T. Nagatsuma, G. Ducournau, and C. C. Renaud, "Advances in terahertz communications accelerated by photonics," Nat. Photonics, vol. 10, no. 6, pp. 371-379, 2016.
- [7] H. Rhee, et al., "Femtosecond characterization of vibrational optical activity of chiral molecules," Nature, vol. 458, no. 7236, pp. 310-313, 2009.
- [8] S. Ghosh, et al., "Broadband optical activity spectroscopy with interferometric Fourier-transform balanced detection," ACS Photonics, vol. 8, no. 8, pp. 2234-2242, 2021.
- [9] J. Shao, et al., "High-precise measurement of optical rotatory dispersion based on weak value amplification," IEEE Photonics I., vol. 13, no. 4, pp. 1-5, 2021.
- [10] Y. Gao, et al., "Chiral terahertz wave emission from the Weyl semimetal TaAs," Nat. Commun., vol. 11, no. 1, p. 720, 2020.
- [11] Z. Tan, F. Fan, D. Zhao, Y. Ji, J. Cheng, and S. Chang, "High-efficiency terahertz nonreciprocal one-way transmission and active asymmetric chiral manipulation based on magnetoplasmon/dielectric metasurface," Adv. Opt. Mater., vol. 9, no. 10, p. 2002216, 2021.
- [12] S. Zhang, et al., "Photoinduced handedness switching in terahertz chiral metamolecules," Nat. Commun., vol. 3, no. 1, p. 942, 2012.
- [13] Z. Zhang, et al., "The novel hybrid metal-graphene metasurfaces for broadband focusing and beam-steering in farfield at the terahertz frequencies," Carbon, vol. 132, pp. 529-538, 2018.
- [14] D. S. Dong, et al., "Terahertz broadband low-reflection metasurface by controlling phase distributions," Adv. Opt. Mater., vol. 3, no. 10, pp. 1405 – 1410, 2015.
- [15] Y. Aharonov, D. Z. Albert, and L. Vaidman, "How the result of a measurement of a component of the spin of a spin-1/2 particle can turn out to be 100," Phys. Rev. Lett., vol. 60, no. 14, p. 1351,
- [16] D. J. Starling, P. B. Dixon, A. N. Jordan, and J. C. Howell, "Precision frequency measurements with interferometric weak values." Phys. Rev. A: At., Mol., Opt. Phys., vol. 82, no. 6, p. 063822, 2010.
- [17] Y. Kedem, "Using technical noise to increase the signal-to-noise ratio of measurements via imaginary weak values," Phys. Rev. A: At., Mol., Opt. Phys., vol. 85, no. 6, p. 060102, 2012.
- [18] G. Jayaswal, G. Mistura, and M. Merano, "Weak measurement of the Goos - Hänchen shift," Opt. Lett., vol. 38, no. 8, pp. 1232-1234,
- [19] Z. Zhang, et al., "All-complex optical field complete imaging scheme via weak measurement," 2024. https://doi.org/10.21203/rs .3.rs-4845650/v1.
- [20] Y. He, et al., "Detection of magneto-optical Kerr signals via weak measurement with frequency pointer," Opt. Lett., vol. 46, no. 17, pp. 4140 – 4143, 2021.
- [21] Y. He, et al., "Manipulating photonic spin accumulation with a magnetic field," J. Appl. Phys., vol. 125, no. 2, 2019. https://doi.org/ 10.1063/1.5058178.
- [22] L. Luo, T. Li, Y. Jiang, L. Fang, B. Liu, and Z. Zhang, "Estimation of Kerr angle based on weak measurement with two pointers," Opt. Express, vol. 31, no. 9, pp. 14432-14441, 2023.

- [23] T. Li, et al., "Observation of the mixed magneto-optical Kerr effects using weak measurement," Opt. Express, vol. 31, no. 15, pp. 24469-24480, 2023.
- [24] Y. Wang, J. Zhu, J. Wu, R. Ge, F. Gao, and Z. Zhang, "High-precision weak measurement sensing with adaptability in sensitivity," Appl. Phys. Lett., vol. 124, no. 13, 2024. https://doi.org/10.1063/5
- [25] T. Li, Y. Wang, Y. Jiang, S. Zhang, L. Luo, and Z. Zhang, "Measurement of the complex polar magneto-optical Kerr effect using weak measurement," arXiv preprint arXiv:2309.13844, 2023.
- [26] J. Liu, et al., "Metasurface-assisted quantum nonlocal weak-measurement microscopy," Phys. Rev. Lett., vol. 132, no. 4, p. 043601, 2024.
- [27] X. Ling, Z. Zhang, Z. Dai, Z. Wang, H. Luo, and L. Zhou, "Photonic spin-hall effect at generic interfaces," Laser Photonics Rev., vol. 17, no. 4, p. 2200783, 2023.
- [28] S. He, et al., "High-order photonic spin Hall effect and its application in high-contrast imaging," Phys. Rev. Appl., vol. 21, no. 3, p. 034045, 2024.
- [29] W. Zhang, Y. Wang, D. Xu, and H. Luo, "Spin-orbit interaction of light: when twisted light meets twisted metasurfaces," Phys. Rev. A, vol. 107, no. 4, p. 043502, 2023.
- [30] Q. Yang, D. Xu, S. Chen, S. Wen, and H. Luo, "Reconstruction of wave function via spin-orbit interaction of light," Phys. Rev. Appl., vol. 20, no. 5, p. 054011, 2023.
- [31] X. Lu, et al., "Weak value amplified precision terahertz spectroscopic detection of solid and liquid glucose samples," ACS Photonics, vol. 10, no. 9, pp. 3149 – 3160, 2023.
- [32] L. Xu, et al., "Measurement of chiral molecular parameters based on a combination of surface plasmon resonance and weak value amplification," ACS Sens., vol. 5, no. 8, pp. 2398 – 2407, 2020.
- [33] L. Xie, et al., "Quantitative detection of the respective concentrations of chiral compounds with weak measurements," Appl. Phys. Lett., vol. 111, no. 19, 2017. https://doi.org/10.1063/1 .5003405.
- [34] L. Xu, et al., "Ultrasensitive optical refractive index detection of NaCl and alcohol solutions based on weak value amplification," Plasmonics, vol. 15, no. 3, pp. 671-678, 2020.
- [35] L. Luo, et al., "Precision improvement of surface plasmon resonance sensors based on weak-value amplification." Opt. Express, vol. 25, no. 18, pp. 21107-21114, 2017.
- [36] R. Wang, et al., "Ultrasensitive and real-time detection of chemical reaction rate based on the photonic spin Hall effect," APL Photonics, vol. 5, no. 1, 2020. https://doi.org/10.1063/1.5131183.
- [37] H. Li, et al., "Real-space sampling of terahertz waveforms under scanning tunneling microscope," ACS Photonics, vol. 11, no. 4, pp. 1428 – 1437, 2024.
- [38] K. Yoshioka, et al., "Real-space coherent manipulation of electrons in a single tunnel junction by single-cycle terahertz electric fields," Nat. Photonics, vol. 10, no. 12, pp. 762-765, 2016.
- [39] S. Yoshida, et al., "Subcycle transient scanning tunneling spectroscopy with visualization of enhanced terahertz near field," ACS Photonics, vol. 6, no. 6, pp. 1356-1364, 2019.
- [40] N. Brunner and C. Simon, "Measuring small longitudinal phase shifts: weak measurements or standard interferometry?," Phys. Rev. Lett., vol. 105, no. 1, p. 010405, 2010.
- [41] X.-Y. Xu, Y. Kedem, K. Sun, L. Vaidman, C.-F. Li, and G.-C. Guo, "Phase estimation with weak measurement using a white light source," Phys. Rev. Lett., vol. 111, no. 3, p. 033604, 2013.

- [42] X. Qiu, et al., "Precision phase estimation based on weak-value amplification," Appl. Phys. Lett., vol. 110, no. 7, 2017. https://doi.org/ 10.1063/1.4976312.
- [43] N. Kakenov, M. S. Ergoktas, O. Balci, and C. Kocabas, "Graphene based terahertz phase modulators," 2D Mater., vol. 5, no. 3, p. 035018, 2018.
- [44] J. Ding, N. Xu, H. Ren, Y. Lin, W. Zhang, and H. Zhang, "Dual-wavelength terahertz metasurfaces with independent phase and amplitude control at each wavelength," Sci. Rep., vol. 6, no. 1, p. 34020, 2016.
- [45] Y.-J. Zhang, et al., "Optical quantum weak measurement coupled with UV spectrophotometry for sensitively and non-separatedly detecting enantiopurity," Opt. Express, vol. 27, no. 7, pp. 9330 - 9342, 2019.
- [46] Y. Zhao, A. N. Askarpour, L. Sun, J. Shi, X. Li, and A. Alù, "Chirality detection of enantiomers using twisted optical metamaterials," Nat. Commun., vol. 8, no. 1, p. 14180, 2017.

- [47] Y. Yuan, et al., "Terahertz characterization of organic crystals using paraffin as dilution matrix," Opt. Mater., vol. 157, p. 116084, 2024.
- [48] W. Liu, et al., "Enhanced chiral sensing in achiral nanostructures with linearly polarized light," Opt. Express, vol. 30, no. 15, pp. 26306-26314, 2022.
- [49] J. Liu, T. Zhang, Z. Tan, J. Cheng, S. Chang, and F. Fan, "Chiral enantiomer recognition of amino acids enhanced by terahertz spin beam separation based on a Pancharatnam - Berry metasurface," Opt. Lett., vol. 48, no. 2, pp. 440-443, 2023.
- [50] M. Hwang, et al., "Lithography-free fabrication of terahertz chiral metamaterials and their chirality enhancement for enantiomer sensing," Adv. Opt. Mater., vol. 11, no. 14, p. 2300045, 2023.

Supplementary Material: This article contains supplementary material (https://doi.org/10.1515/nanoph-2024-0685).